ATP-dependent DNA binding, unwinding, and resection by the Mre11/Rad50 complex

Yaqi Liu[1,†], Sihyun Sung[1,†], Youngran Kim[1,†], Fuyang Li[2,3], Gwanghyun Gwon[1], Aera Jo[1], Ae-Kyoung Kim[4], Taeyoon Kim[1], Ok-kyu Song[4], Sang Eun Lee[2,3] & Yunje Cho[1,*]

Abstract

ATP-dependent DNA end recognition and nucleolytic processing are central functions of the Mre11/Rad50 (MR) complex in DNA double-strand break repair. However, it is still unclear how ATP binding and hydrolysis primes the MR function and regulates repair pathway choice in cells. Here, *Methanococcus jannaschii* MR-ATPγS-DNA structure reveals that the partly deformed DNA runs symmetrically across central groove between two ATPγS-bound Rad50 nucleotide-binding domains. Duplex DNA cannot access the Mre11 active site in the ATP-free full-length MR complex. ATP hydrolysis drives rotation of the nucleotide-binding domain and induces the DNA melting so that the substrate DNA can access Mre11. Our findings suggest that the ATP hydrolysis-driven conformational changes in both DNA and the MR complex coordinate the melting and endonuclease activity.

Introduction

DNA double-strand breaks (DSBs) is one of the most detrimental types of DNA damage, which can be repaired via homologous recombination (HR) or non-homologous end-joining (NHEJ) repair pathway (Symington & Gautier, 2011). The Mre11/Rad50/Nbs1 (MRN) complex in mammals (the Mre11/Rad50/Xrs2 (MRX) complex in *Saccharomyces cerevisiae*) plays a central role in DSB repair by recognizing and resecting the damaged DNA ends, and transducing a signal via activation of ataxia telangiectasia mutated (ATM) kinase (Stracker & Petrini, 2011; Lafrance-Vanasse *et al*,

2015). In addition, MRN complex plays a crucial role in telomere maintenance, meiotic recombination, and class switch recombination in B cells (Boulton & Jackson, 1998; Furuse *et al*, 1998; Moreau *et al*, 1999; Reis *et al*, 2012). The importance of MRN function to DNA metabolism is underscored by the fact that deletion of any of its three components leads to embryonic lethality in mice, and hypomorphic mutations in MRN components result in various developmental and neurodegenerative disorders (Varon *et al*, 1998; Stewart *et al*, 1999; Buis *et al*, 2008; Waltes *et al*, 2009).

In the MR complex, Mre11 dimer is responsible for Mn^{2+}- or Mg^{2+}-dependent nuclease activities, which include 3′–5′ exonuclease, endonuclease, and hairpin opening activities (Connelly *et al*, 1997; Paull & Gellert, 1998; Hopfner *et al*, 2000a,b; Trujillo & Sung, 2001; Williams *et al*, 2008; Park *et al*, 2011; Schiller *et al*, 2012). Bacterial homolog of the Mre11/Rad50 complex, SbcD/SbcC, also cleaves the hairpins at inverted repeats and facilitates the replication restarts (Darmon *et al*, 2010). At the initial stages of DSB repair and meiotic recombination, the yeast MRX complex together with Sae2 nicks the DNA at a set distance from the damaged end, and this process is followed by 3′–5′ resection toward the DSB (Limbo *et al*, 2007; Garcia *et al*, 2011; Cannavo & Cejka, 2014; Shibata *et al*, 2014). Other nucleases, such as Exo1 or BLM/Dna2, perform further resection in the 5′–3′ direction, away from the DSB (Mimitou & Symington, 2008; Zhu *et al*, 2008; Cejka *et al*, 2010). These nuclease activities are crucial for removing obstructed DNA ends for HR (Liu *et al*, 2002; Neale *et al*, 2005).

Rad50 is an ATP-binding cassette ATPase that has two lobes, each of which contains Walker A and B motifs. Rad50 shares a similar head domain (nucleotide-binding domain, NBD) with members of the structural maintenance of chromosomes (SMC) family (Hopfner *et al*, 2000a,b). ATP-binding and hydrolysis activities of Rad50 are crucial for binding, unwinding, and tethering of the DNA ends, as well as for ATM kinase activation and regulating the endonuclease activity of the MR complex (Raymond & Kleckner, 1993; Paull & Gellert, 1999; Chen *et al*, 2005; Lee & Paull, 2005; Deshpande *et al*, 2014).

Two MR complexes form an elongated shape that can be further divided into ATPase head, zinc-hook domain, and a long antiparallel coiled-coil arm that connects the head and the hook

1   Department of Life Sciences, Pohang University of Science and Technology, Pohang, South Korea
2   Department of Molecular Medicine, Institute of Biotechnology, University of Texas Health Science Center at San Antonio, San Antonio, TX, USA
3   Department of Radiation Oncology, University of Texas Health Science Center at San Antonio, San Antonio, TX, USA
4   Panbionet Corporation, Pohang, South Korea
    *Corresponding author. Tel: +82 54 279 2288; E-mail: yunje@postech.ac.kr
    †These authors contributed equally to this work

domains (Hopfner *et al*, 2001, 2002; de Jager *et al*, 2001; Moreno-Herrero *et al*, 2005). The head region contains two Rad50 ATPase domains and two Mre11 nuclease proteins. The coiled-coil region of Rad50 at the base of the ATPase head interacts with the C-terminal three helix-bundle (or helix-loop-helix) of Mre11 (Lammens *et al*, 2011; Lim *et al*, 2011; Williams *et al*, 2011; Möckel *et al*, 2012).

Structural analyses of prokaryotic MR catalytic domain (MRcd) lacking the coiled-coil region and zinc-hook domain have shown that ATP binding and hydrolysis switches the conformation of the MR complex. Head region of MR tetramer complex forms a closed state in the presence of ATP, in which the two Rad50 ATPase domains engage to sandwich two ATP molecules and occlude the active site of Mre11 nuclease dimer (Lim *et al*, 2011; Möckel *et al*, 2012). ATP hydrolysis drives the rotation of the two lobes of Rad50 as much as 30° and leads to disengagement of Rad50 dimer, which allows DNA to enter the Mre11 active site for resection (Lammens *et al*, 2011). This ATP-dependent conformational change regulates nuclease activity of the MR complex. Based on structural and biochemical data, it has been proposed that the ATP-bound MR complex with a closed head domain is important for directing the NHEJ pathway, whereas the ATP-free MR complex with an open head domain directs HR repair (Deshpande *et al*, 2014).

Despite an elegant model how ATP binding and hydrolysis induces the conformation change of the MR complex, it does not fully explain biochemical properties of ATP-free MR. For example, based on the open conformation of ATP-free MRcd complex, this MR complex should still be able to cleave its substrate DNA even in the absence of ATP because there is no restriction in accessing dsDNA to Mre11. Surprisingly, the full-length prokaryotic MR complex or eukaryotic MRN/X complex does not exhibit endonuclease activity in the absence of ATP (Connelly *et al*, 1997; Hopfner *et al*, 2000a,b; Lee *et al*, 2003; Chen *et al*, 2005; Deshpande *et al*, 2014). These studies thus indicate that the ATP-free intact MR complex may adopt a conformation, which could be different from the open conformation of the ATP-free MRcd complex. In this case, it is unclear how the substrate DNA can access the Mre11 active site in the full-length MR complex, and how ATP promotes the DNA unwinding and endonuclease activities of the MR complex.

Here, by using structural, biochemical, and genetic approaches, we examined a binding model for the ATPγS-bound MR and DNA complex. Crystal structure of the ATPγS–MR–DNA complex revealed that double-stranded (ds) DNA binds to the central groove at the dimeric interface of Rad50 dimer in a partly deformed conformation. DNA binding analyses suggest that the full-length nucleotide-free MR complex forms an ATPase head arrangement, different from that of the coiled-coil deleted MRcd complex, in such a way that dsDNA cannot access Mre11. ATP hydrolysis triggers the conformational change and the domain rotation of Rad50, which subsequently melts the dsDNA. Biochemical analyses showed that a bubble but not intact duplex DNA can be cleaved by Mre11 in the ATP-free state, suggesting that ATP-dependent DNA binding, DNA melting, and Rad50 dimer disengagement are all essential for the efficient resection of DNA ends by the MR complex. Based on the integrative approach, we propose a new model by which the ATP hydrolysis-driven concerted motion of Rad50 and Mre11 couples the DNA binding and melting by Rad50 to endonucleolytic cleavage by Mre11 in DSB repair process.

Results

Overall structure of the ATPγS–MR–DNA complex

To understand how ATP promotes the MR complex to recognize the DNA, we determined the structure of the ATPγS–MR–DNA complex. We crystallized the complex containing *Methanococcus jannaschii* (*Mj*) Mre11 (full-length) and Rad50 ATPase domain (residues 1–190 and 825–1,005) in the presence of ATPγS and a 25-base pair (bp) dsDNA containing 2-nt 5′ overhangs (Fig 1A and B). The crystal contains two molecules of the MR complex in the asymmetric unit, which are arranged in an ATPγS-bound MR tetramer similar to that described previously (Lim *et al*, 2011; Möckel *et al*, 2012). The 3.1 Å resolution electron density map revealed a 22-bp dsDNA with a 3-nt overhang at one 5′ end and a 1-nt overhang at the other 5′ end, which runs across the central groove at the interface of Rad50 dimer, with its central axis tilted approximately 15° relative to the dimer interface (Fig 1C and D, Table 1, Appendix Fig S1, Movie EV1).

The 38-Å-long and 25-Å-wide central groove at Rad50 dimeric interface is formed only in the presence of ATP or an analogue (Figs 2A and EV1, Hopfner *et al*, 2000a,b; Lim *et al*, 2011; Williams *et al*, 2011; Möckel *et al*, 2012). The DNA duplex interacts with the Rad50 ATPase dimer in a near-symmetrical manner. Both Rad50 monomers bind to each end of the DNA strand via three motifs, namely loops α1-α2, β7-α3, and β5-β6 at the N-terminal lobe (or lobe I, residues 1–137 and 939–1,005) (Fig 2A–C). We refer to each Rad50 ATPase domain as Rad50 A (green) and Rad50 B (blue) and each DNA strand as "template" (orange) and "non-template" (yellow) (Fig 2A and E). The structure of the DNA bound at the central groove of Rad50 dimer is consistent with previous modeling-based prediction, as well as functional studies showing that ATP binding-induced dimerization is important for DNA binding (Raymond & Kleckner, 1993; Hopfner *et al*, 2000a,b, 2001; Lim *et al*, 2011; Rojowska *et al*, 2014).

ATP-dependent symmetric DNA recognition by the MR complex

Rad50-DNA contacts occur primarily between phosphate groups and protein side-chain groups in a sequence-independent manner (Movie EV2). Interactions between one Rad50 molecule (Rad50 A) and one end of the DNA strand are similar to those between another Rad50 molecule (Rad50 B) and the opposite end of the DNA strand (Fig 2B–E). The most noticeable features are loop α1-α2 (residues 51–58), which wedges the minor groove and loop β5-β6, which protrudes into the major groove (Fig 2B and C). Three successive phosphate groups in the minor groove interact with lobe I. Asn57 and the main chain of Tyr58 bind to the first phosphate group (Cyt8′), Ala52 (main-chain) and Tyr58 interact with the second phosphate group (Cyt7′), and Thr107 and Ser109 recognize the Ade6′ phosphate group. Arg92 side chain interacts with the Ade5′ and Gua4 bases in the major groove (Fig 2B and E). A conserved Arg86 is located near the Cyt7′ phosphate (4.2 Å), and its guanidinium group stacks against the backbone of loop α1-α2 and interacts with Asn112, thereby stabilizing the two DNA-interacting loops, α1-α2 and β7-α3. Interaction between Rad50 and DNA in the complex structure is reinforced by the cluster of positively charged residues along the groove, as supported by mutational analyses of Rad50 (Fig EV1B; Lim *et al*, 2011; Rojowska *et al*, 2014).
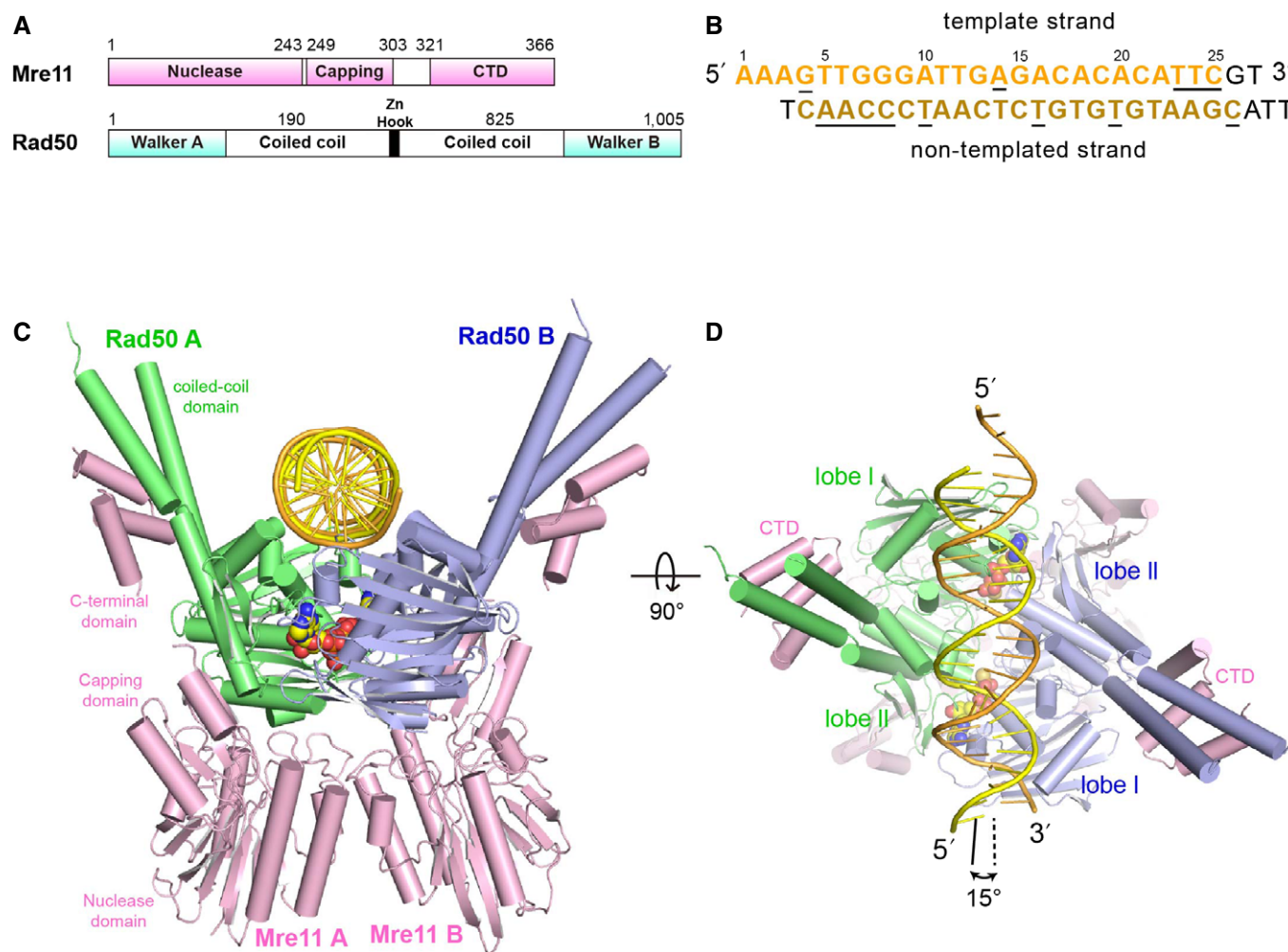
Figure 1. Overall structure of the ATPγS–MR–DNA complex.

A Schematic diagram of the domain organizations of Mre11 (top) and Rad50 (bottom).

B The 25-bp duplex DNA with 2-nt 5′ overhangs used in the crystallization. The two strands are labeled as "template" (orange, top) and "non-template" (dark yellow, bottom). In the text, bases are numbered from the 5′ end of the "template" strand, and bases of the "non-template" strand are denoted by base pair numbers followed by the prime (′) symbol. Disordered residues are shown in black. The protein-contacting residues are underlined.

C A ribbon representation of the 3.1-Å ATPγS–*Mj*MR–DNA structure showing the Mre11 nuclease, capping, and C-terminal three helix-bundle domain (light pink), Rad50 molecules (green and light blue), and the DNA (yellow and orange). ATPγS is shown in spheres. See Movie EV1 for the movement of the complex.

D Orthogonal view of the complex. Lobes I and II in each Rad50 monomer are labeled. The angle between the dimeric interface of two NBDs and the central axis of DNA is also shown.

Comparison of two different DNA binding modes by the nucleotide-bound MR complex

Recently determined structure of the *Thermotoga maritima* (*Tm*) Rad50 nucleotide-binding domain (NBD) complexed with the C-terminal motif of *Tm*Mre11 and a 15-bp dsDNA (4W9M) revealed a mechanism by which β-γ-imidoadenosine 5′-phosphate (AMP-PNP)-bound Rad50 dimer recognizes the DNA (Rojowska *et al*, 2014). In *Tm*Rad50-DNA structure, DNA binds to only one of the two Rad50 NBDs, mainly to a strand-loop-helix at the N-terminal lobe (equivalent to β7-loop-α3 of *Mj*MR) with additional contact with the coiled-coil region. The overall location and orientation of DNA within *Tm*Rad50 markedly differ from those within *Mj*MR (Fig EV2). The presence of two different binding sites for DNA from the two structures can be interpreted

that Rad50 may interact with DNA through multiple sites in the head domain.

Although most of the residues interacting with DNA via their side chains are polar or charged, they are not conserved in three available prokaryotic Rad50 structures (Fig 2D and E). Weak conservation of the DNA-binding residues at the central groove suggests that these residues in Rad50 molecules from various species may contribute differently in DNA recognition. Upon DNA binding, a 1,945 Å² surface area of *Mj*Rad50 becomes buried, whereas a 500 Å² area is buried in *Tm*Rad50, suggesting that symmetric DNA recognition by *Mj*Rad50 involves more extensive contacts than asymmetric binding. Alternatively, difference in DNA binding between two structures may be attributed to the differences in the DNA length used in the crystallization. The distance between each α1-α2 loops in the *Mj*Rad50 dimer is about 18 bp (Fig 2A).

Table 1. Data collection and refinement statistics.

	ATPγS–*Mj*MR–DNA
Data collection	
Space group	P2$_1$2$_1$2$_1$
Cell dimensions	
a, b, c (Å)	84.3, 130.1, 166.6
α, β, γ (°)	90, 90, 90
Resolution (Å)	50–3.1 (3.18–3.1)[a]
Measured reflections	203,911
Unique reflections	32,303
Completeness (%)	96.4 (97.0)
Average (*I*/σ)	18.7 (1.6)
R_{merge} (%)	0.158 (2.06)
CC1/2[b]	0.996 (0.397)
Redundancy	6.3 (6.5)
Wilson B-factors (Å^2)	95.3
Refinement	
Resolution (Å)	40.87–3.1
No. reflections	32220
R_{work}/R_{free} (%)[c]	22.2/26.9
No. atoms	
Protein	11606
DNA/ATPγS	984/62
Mg^{2+}/water	4/2
B-factors	
Protein	109.3
DNA/ATPγS	154.7/129.3
Mg^{2+}/water	88.5/72.1
R.m.s deviations	
Bond lengths (Å)	0.003
Bond angles (°)	0.54
Clash score[d] Ramachandran Plot[d]	7.2
Most favored (%)	92.9
Allowed (%)	7.1
Disallowed (%)	0

[a]Values in parentheses are for the highest shell.
[b]Karplus and Diederichs (2012).
[c]$R = |F_{obs}\text{-}F_{calc}|/F_{obs}$, where $F_{obs} = F_{pi}$ and F_{calc} is the calculated protein structure factor from the atomic model (R_{free} was calculated with 5% of the reflections).
[d]Clash score and Ramachandran plot are calculated by Molprobity (Chen *et al*, 2010).

Full-length and truncated MR complexes exhibit different DNA-binding patterns

To validate the DNA binding by the ATPγS–*Mj*MR complex observed in the crystal structure, we introduced four mutations (Δ53–55 (deletion of 53–55), R86E, R92E, and T107E, Figs 2B and 3A) into the residues of *Mj*Rad50 that likely contribute to DNA

contact or their immediate vicinity, and examined the DNA binding activities of the *Mj*MRcd (residues 1–190 and 825–1,005) mutants using a closed circular dsDNA (φx174RFII). Interestingly, all *Mj*MRcd wild-type and mutants exhibited similar robust DNA binding activities in the nucleotide-free condition (Fig 3B). Because *Pyrococcus furiosus* (*Pf*) Rad50cd interacted with DNA only in the presence of a nucleotide (Hopfner *et al*, 2000a,b), these results suggest that DNA binding in AMP-PNP-free condition is primarily contributed by *Mj*Mre11 and therefore is not dependent on the binding activity by Rad50. This interpretation is consistent with the reported structure, in which DNA-binding surface of Mre11 is open in the nucleotide-free MRcd complex (Lammens *et al*, 2011). In the presence of AMP-PNP and Mg^{2+}, all *Mj*MRcd mutants (R86E, R92E, and T107E) except for *Mj*MRcd (Δ53–55) exhibited significantly reduced binding to the DNA relative to wild-type (WT) *Mj*MRcd (Fig 3C). We used AMP-PNP instead of ATPγS, because weak but residual hydrolyzing property of ATPγS might activate the MR nuclease activity, and interfere for an accurate detection of DNA binding to the mutants. The results validate our structure and the proposed DNA-binding interface as critical for binding of Rad50 to DNA (Hopfner *et al*, 2001; Lim *et al*, 2011).

MRcd lacks the essential coiled-coil and zinc-hook domains, which could restrict the movement of the Rad50 ATPase head as proposed by Lee *et al* (2013). It is therefore of a significant interest if the full-length MR complex forms a similar conformation as that of the MRcd and exhibits the nucleotide dependent and independent DNA binding pattern as shown in Fig 3B and C. We thus examined the DNA binding activity of the full-length MR complex. Full-length *Mj*MR cannot be produced in soluble form; therefore, we used full-length *Tm*MR proteins. Unlike *Mj*MRcd wherein ATP-free form binds to DNA independently of Rad50 mutations, both a nucleotide-free and nucleotide-bound full-length *Tm*MR cannot efficiently bind to DNA if Rad50 harbors mutations at Arg87, Lys95, and Lys115 (Fig 3D and E). Lys115 of *Tm*Rad50 is equivalent to Thr107 of *Mj*Rad50 in aligned structures. The K115E *Tm*MR mutant binds to DNA at high protein to DNA ratio. Both ATP-free and ATP-bound forms of wild-type or each mutant *Tm*MR proteins exhibit similar DNA binding activities and patterns. We observed similar DNA binding patterns between MRcd (or full-length MR) and a linear DNA (pCDFDuet-1 cleaved by EcoRI, Fig EV3A–D). All of Rad50 mutants used here retained full ATPase activities (Appendix Fig S2). The results raise the possibility that the structure of full-length MR is different from that of MRcd and the coiled-coil and zinc hook restrict the NBD movement of the nucleotide-free MR complex. We propose that the NBDs of nucleotide-free full-length MR are arranged in such a way the access of dsDNA to Mre11 is impeded (see Discussion for further details).

To test this idea further, we compared the nuclease activities of free Mre11, ATP-unbound and ATP-bound MRcd and the full-length MR using hairpin DNA as a substrate (Fig 3F and G). We surmised that nucleotide-free MRcd retains the ability to cleave hairpin DNA to the level identical or similar to free Mre11 because the active site of Mre11 in the MRcd complex is not blocked and open for the cleavage. By contrast, the nucleotide-free full-length MR complex exhibits no or weak nuclease activity because Rad50 prevents the access of DNA to Mre11 in nucleotide-free condition. Indeed, the nucleotide-free *Mj*MRcd complex exhibits a hairpin-cleavage activity comparable to that of the Mre11 alone. Most importantly, the
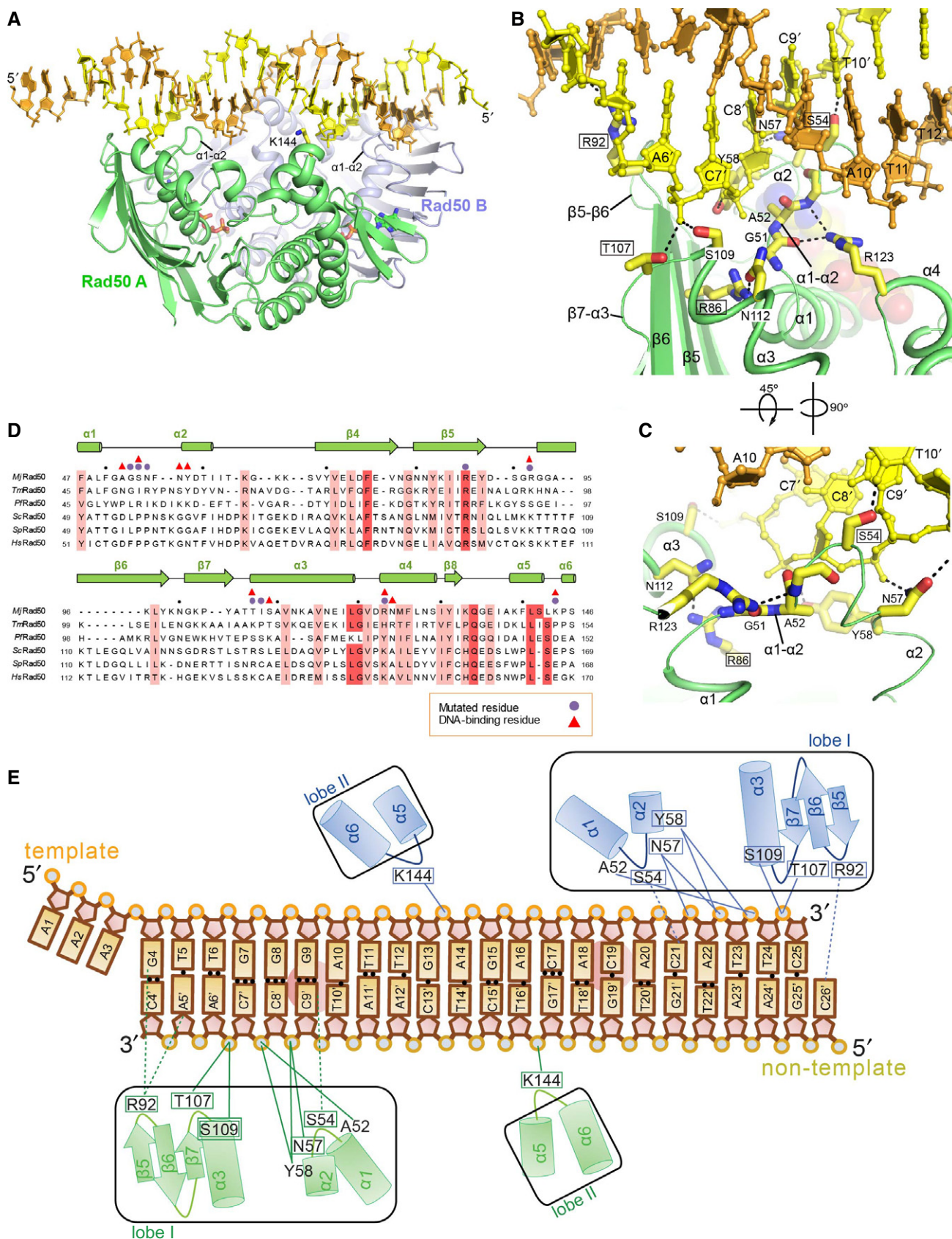
Figure 2.

Figure 2. Close-up view of the interactions between the MR complex and the DNA substrate.

A   A ribbon diagram showing the overall DNA recognition by the ATPγS–Rad50 dimer.

B   Close-up view of the interaction between the internal segment (major and minor grooves) of the DNA strand and the edge of lobe I of Rad50A (green). Loop α1–α2 wedge faces the minor groove between the 10th and 13'th phosphates of the template (orange) and non-template (yellow) strands, respectively.

C   Close-up view of the interaction between the DNA strand and the α1–α2 loop in an orientation different from (B).

D   Structure-based sequence alignment of the N-terminal domains of Rad50 orthologues. The organisms are *Methanococcus jannaschii* (Uniprot ID, Q58718), *Thermotoga maritima* (Q9X1X1), *Pyrococcus furiosus* (P58301), *Saccharomyces cerevisiae* (P12753), *Schizosaccharomyces pombe* (Q9UTJ8), and *Homo sapiens* (Q92878). Strictly conserved and highly conserved residues are highlighted in red and pale red, respectively. Every 10th residue is marked with a black dot. The Rad50 residues mutated in this study are highlighted with purple circle. DNA-binding residues are indicated by red triangles. Sequence alignment was performed using Clustal X (Larkin *et al*, 2007).

E   A cartoon of the molecular details of the ATP-dependent Rad50 dimer–DNA interaction. Schematic illustrations of all direct *Mj*Rad50 dimer–DNA interactions show that DNA recognition by Rad50 dimer is symmetrical. The phosphate group is marked with a closed circle. Hydrogen bonds and ion pairs between *Mj*MR and the DNA molecule are indicated by blue and green lines. Bases are numbered as in Fig 1B. Residues that interact with DNA via side chain are boxed, and via main chain (Ser109) is shown in two green boxes.

nucleotide-free full-length MR exhibits virtually null (or very weak) hairpin-cleavage activity. Addition of ATP significantly increases endonuclease activity of the full-length *Tm*MR protein. ATP did not stimulate endonuclease activity of the *Mj*MRcd complex (Fig 3F; Lim *et al*, 2011). We concluded that coiled-coil and zinc-hook domain of Rad50 are critical in regulating the nuclease activity of Mre11 under ATP-dependent manner, consistent with the reported studies (see Discussion, Lee *et al*, 2013; Hohl *et al*, 2015; Barfoot *et al*, 2015).

Conformation of a DNA bound to the ATPγS–MR complex

In the *Mj*MR-DNA complex, the α1–α2 and β5–β6 loops sandwich the 3rd to 6th phosphates of the template strand, which results in a partly deviated strand from its ideal B-form (Figs 2B and EV4A and B). The width of the minor groove (distance between the 7'th and 12th phosphate groups), which is wedged by loop α1–α2, increases from 13.2 Å (for B-form DNA) to 15.3 Å. A major groove at the center flanked by the minor grooves at both sides is constricted to 17.3 Å (distance between the 12th and 17'th phosphate groups; 20.6 Å for B-form DNA), with a small kink (approximately 7°, Fig EV4). The width between the two strands also increases. Distance between the 11'th and 12th phosphate groups changes to 18.4 Å from 17.3 Å upon binding to Rad50.

DNA binding induces rotation of the coiled-coil arm of Rad50

ATPγS-bound *Mj*MR also undergoes conformational changes upon binding to DNA. Superposition of apo-*Mj*MR (3AV0, magenta in Fig 4A) and ATPγS–*Mj*MR–DNA (green) by aligning an NBD reveals notable differences in the orientation of the coiled-coils, which are rotated inward by 27° and become more parallel in the DNA-bound *Mj*MR structure (Fig 4A). This is consistent with the time-resolved atomic force microscope analysis of the human MRN–DNA complex (Moreno-Herrero *et al*, 2005). In a close-up view, helix α6 slides toward the DNA (by 1.5 Å for 14 Cα atoms), which shifts Lys144 to interact with phosphate backbone (Fig 4B and C). Translation of helix α6 moves Leu155 and Leu156 to pack tightly against the hydrophobic pocket formed between lobe I and lobe II (Fig EV5A and B). Also, a new ion-pair network (Asp159, Lys163, Arg939) is formed, which interacts with main chain of Gly120 (Fig EV5C and D). These structural transitions would stabilize the rotated coiled-coils in the DNA-bound *Mj*MR structure. In addition, loop α1–α2 is rearranged into a more compact form to fit into the minor groove of DNA (Fig EV5E).

Basis for ATP-dependent DNA melting by Rad50

Because DNA is positioned at the interface of Rad50 dimer, ATP hydrolysis could rotate each lobe to deform the DNA strand further. Two lobes of Rad50 can be rotated up to 30° upon ATP hydrolysis (Hopfner *et al*, 2000a,b; Lim *et al*, 2011; Williams *et al*, 2011). To understand how ATP hydrolysis affects the DNA conformation, we superimposed ADP-*Mj*Rad50 (3AUX) and the ATPγS–*Mj*MR–DNA complex structures by aligning their lobe II domains (1.1 Å rmsd in 66 Cα positions). The superimposed structures reveal the gross movement (as much as 26 Å) of the α1–α2 loop, in such a way that this loop could collide with a few DNA residues during the conformational change (Fig 5A, Movie EV3). In addition, rotation of lobe I shifts the positions of the β5–β7 strands as much as 27 Å and opens the gate for Mre11 (Fig 5B).

To determine whether domain rotation of Rad50 melts DNA, we examined DNA unwinding activity of a *Tm*MR complex containing a nuclease-inactive (H94S) Mre11 variant on 50-bp dsDNA. The experiment was not performed at the optimal temperature for the enzyme activity (55°C) as significant portions of the control DNA would be melted at this temperature. Thus, we performed the unwinding analysis at 25°C to compare relative dsDNA unwinding activities of various *Tm*MR complexes. Prokaryotic MR complex failed to melt DNA in the absence of ATP or in the presence of ATPγS (Fig 5C). By contrast, the addition of ATP stimulated the melting activity of *Tm*MR. WT *Tm*MR exhibited a limited DNA unwinding activity (~8%), which is similar to the unwinding activity of the human MRN complex (Paull & Gellert, 1999). Unlike the human complex, which can only melt short (17 bp) dsDNA molecule, the prokaryotic MR complex lacking Nbs1 can unwind much longer DNA strands (Paull & Gellert, 1999). The *Tm*MR (Δ54–56) mutant exhibited slightly reduced DNA unwinding activity, whereas the other mutants showed almost no DNA melting activity (Figs 3A and 5D). This finding suggests that ATP-dependent partial DNA unwinding activity is conserved in both prokaryotic MR and eukaryotic MRN complexes (Paull & Gellert, 1999; Chen *et al*, 2005; Cannon *et al*, 2013).

Coupling of DNA melting activity of Rad50 and *in vitro* endonuclease activity of Mre11

Next, we investigated whether ATPase-driven DNA melting by the MR complex stimulates endonuclease activity of Mre11. As predicted, WT *Tm*MR exhibited ATP-dependent nuclease activity toward an 81-bp DNA strand at both 25 and 55°C (Fig 6A, Appendix Figs S3 and S4). Four *Tm*MR mutants (Rad50 Δ54–56,

A

	Mutated residue(s)				
*Mj*Rad50	Δ53-55	R86E	R92E		T107E
*Tm*Rad50	Δ54-56	R87E	K95E	R94E/K95E	K115E
*Sc*Rad50	Δ55-57	R96E	K104E	K103E/K104E	R131E

B *Mj*MRcd - dsDNA (− AMP-PNP/Mg^{2+})

C *Mj*MRcd - dsDNA (+ AMP-PNP/Mg^{2+})

D *Tm*MR - dsDNA (− AMP-PNP/Mg^{2+})

E *Tm*MR - dsDNA (+ AMP-PNP/Mg^{2+})

F

DAR134

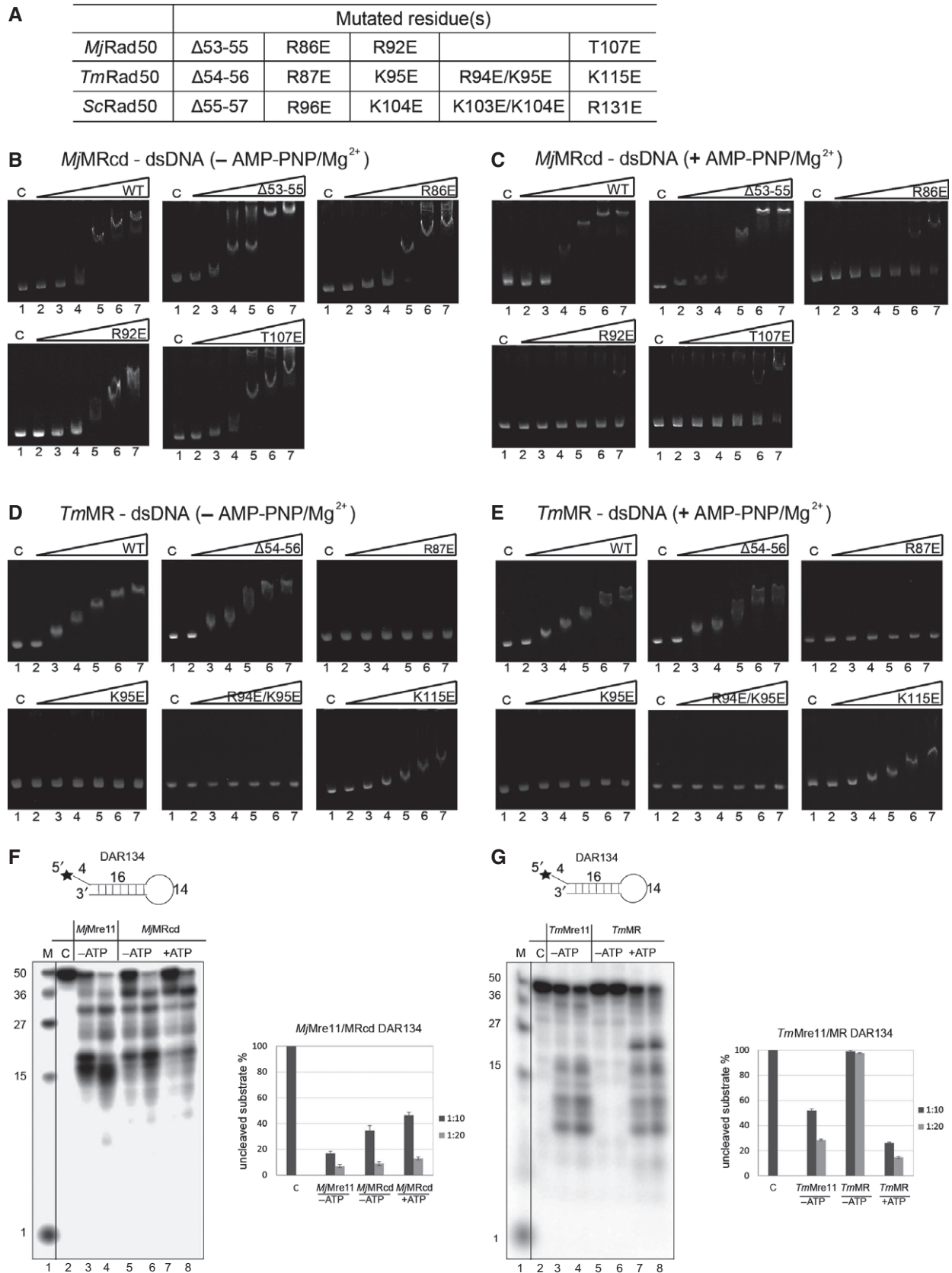*Mj*Mre11/MRcd DAR134

G

DAR134

*Tm*Mre11/MR DAR134

Figure 3.

Figure 3. DNA binding activities of various AMP-PNP-free and AMP-PNP-bound MR proteins.

A   A list of the Rad50 mutants used in this study.

B, C   DNA binding analysis for the interactions between WT or four *Mj*MRcd mutants and a closed circular dsDNA (φx174RFII) in the absence (B) or presence (C) of AMP-PNP/Mg²⁺. Each protein sample was incubated with φx174RFII dsDNA (3.5 nM) for 30 min on 4°C. We note that some MRcd variants may form a second form of the complex with DNA.

D, E   Interactions of the WT or five full-length *Tm*MR mutants with φx174RFII were examined in the absence (D) or presence of AMP-PNP/Mg²⁺ (E). Reaction conditions as in (B, C).

F   Nuclease activities of free *Mj*Mre11 (lane 3, 4), nucleotide-unbound (lane 5, 6) and nucleotide-bound *Mj*MRcd complex (lane 7, 8) toward a hairpin DNA. Each protein sample was incubated with a hairpin DNA (10 nM) in a 1:10 or 1:20 molar ratio (protein: DNA) for 30 min on 55°C. The error bars for the quantified values of uncleaved substrates on the right panel are calculated from the standard deviation from three repetitions of each experiment.

G   Nuclease activities of free *Tm*Mre11 alone (lane 3, 4), nucleotide-unbound (lane 5, 6) and nucleotide-bound (lane 7, 8) full-length *Tm*MR complex toward a hairpin DNA.

Data information: The following molar ratio of protein:DNA is used in (B–E): lane 2, 50:1; lane 3, 100:1; lane 4, 200:1; lane 5, 500:1; lane 6, 1,000:1; lane 7, 2,000:1.
Source data are available online for this figure.

R87E, R94E/R95E, and R95E, see Fig 3A for corresponding residues in other species) exhibited no or weak endonuclease activities in the absence or presence of ATP, suggesting that the DNA binding activities of Rad50 are important for the resection by Mre11 (Figs 3B–E and 6A). The *Tm*MR complex containing the Rad50 Δ54–56 mutant did not cleave dsDNA, even if it retains limited DNA unwinding activities. Possibly, relatively weak DNA unwinding activities of the *Tm*MR (Δ54–56) complex may not be sufficient for robust endonucleolytic cleavage.

One intriguing possibility is that Rad50- and ATP-dependent DNA melting facilitates the access of Mre11 for DNA cleavage. The model explains as to how cells couple ATP hydrolysis to nuclease activity of Mre11 in full-length *Tm*MR. In the superimposed ADP-*Mj*Rad50 and ATPγS–*Mj*MR–DNA complex structures, the lobe I of the ADP-*Mj*Rad50 shifts as much as 27 Å, which could allow the access of ssDNA to Mre11 (Fig 5B). To test this idea further, we examined the binding and nuclease activities of WT and mutant *Tm*MR complexes toward a substrate containing a 15-nt bubble at the middle of the 81-bp dsDNA. All *Tm*MR

proteins interacted with the bubble DNA, although mutants exhibited reduced bubble DNA binding activities compared to that of WT *Tm*MR (Figs 6B and EV3E and F). All *Tm*MR mutants exhibited significantly higher endonuclease activities toward the bubble substrate than toward the intact 81-bp dsDNA in the absence of ATP (Fig 6A and C, left panel). The mutants generated approximately 23-nt and 33-nt fragments due to the cleavage at or near the bubble site, which differed from the cleavage product of the duplex substrate produced by WT *Tm*MR (Fig 6C, left panel). The addition of ATP strongly stimulated WT *Tm*MR to produce 13-nt, 20-nt, 23-nt, and 33-nt fragments as major products (Fig 6C, right panel). By contrast, ATP did not stimulate the nuclease activities of the *Tm*MR mutants. These findings suggest that unwound DNA but not intact dsDNA could access the Mre11 active site for DNA cleavage, which is stimulated by ATP binding and hydrolysis of Rad50.

For unknown reasons, WT *Tm*MR produced fragments of approximately 13 nt and 20 nt as major products in the presence of ATP. The dsDNA cleavage by the MR complex occurs in a symmetrical
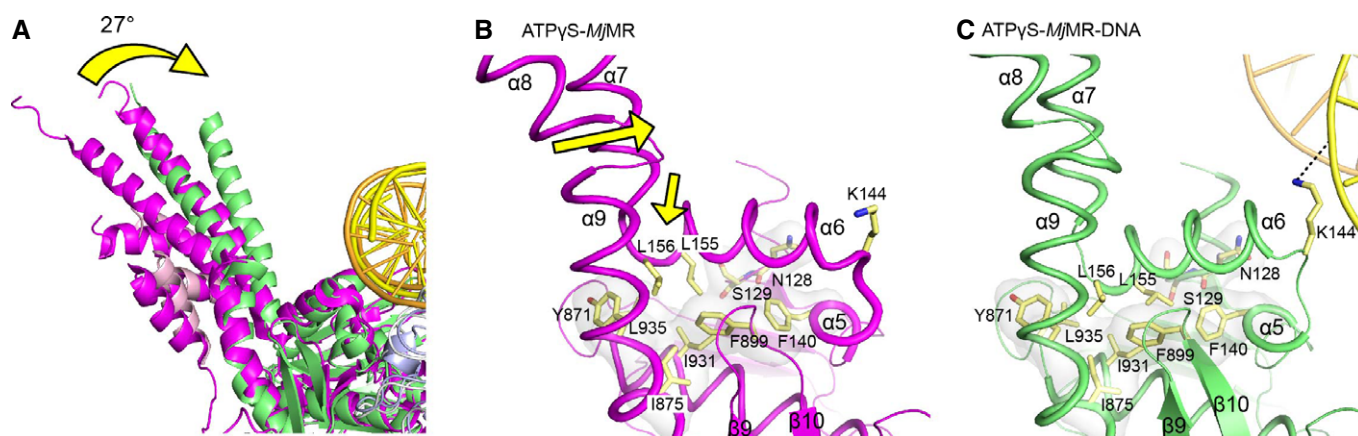
Figure 4. DNA binding-induced structural transition of the *Mj*MR complex.

A   Superposition of the ATPγS–*Mj*MR–DNA complex (green) and apo-*Mj*MR (3AV0, magenta) structures. Alignment was done using their NBDs (1.3 Å rmsd in the positions of 311 Cα atoms). The coiled-coils of the DNA-bound Rad50 molecules are shifted (arrow) to more parallel orientation. The entire structures can be superimposed with a 1.9-Å rmsd in 692 Cα positions.

B, C   Comparison of the local structures between the apo (B) and the DNA-bound *Mj*MR complex (C). Upon DNA binding, helix α6 translates to DNA backbone, resulting in the tighter packing of Leu155 and Leu156 against a hydrophobic pocket formed by lobe I and II. Arrows indicate the direction of the helix movement by DNA binding. See Fig EV5 for a close-up view.
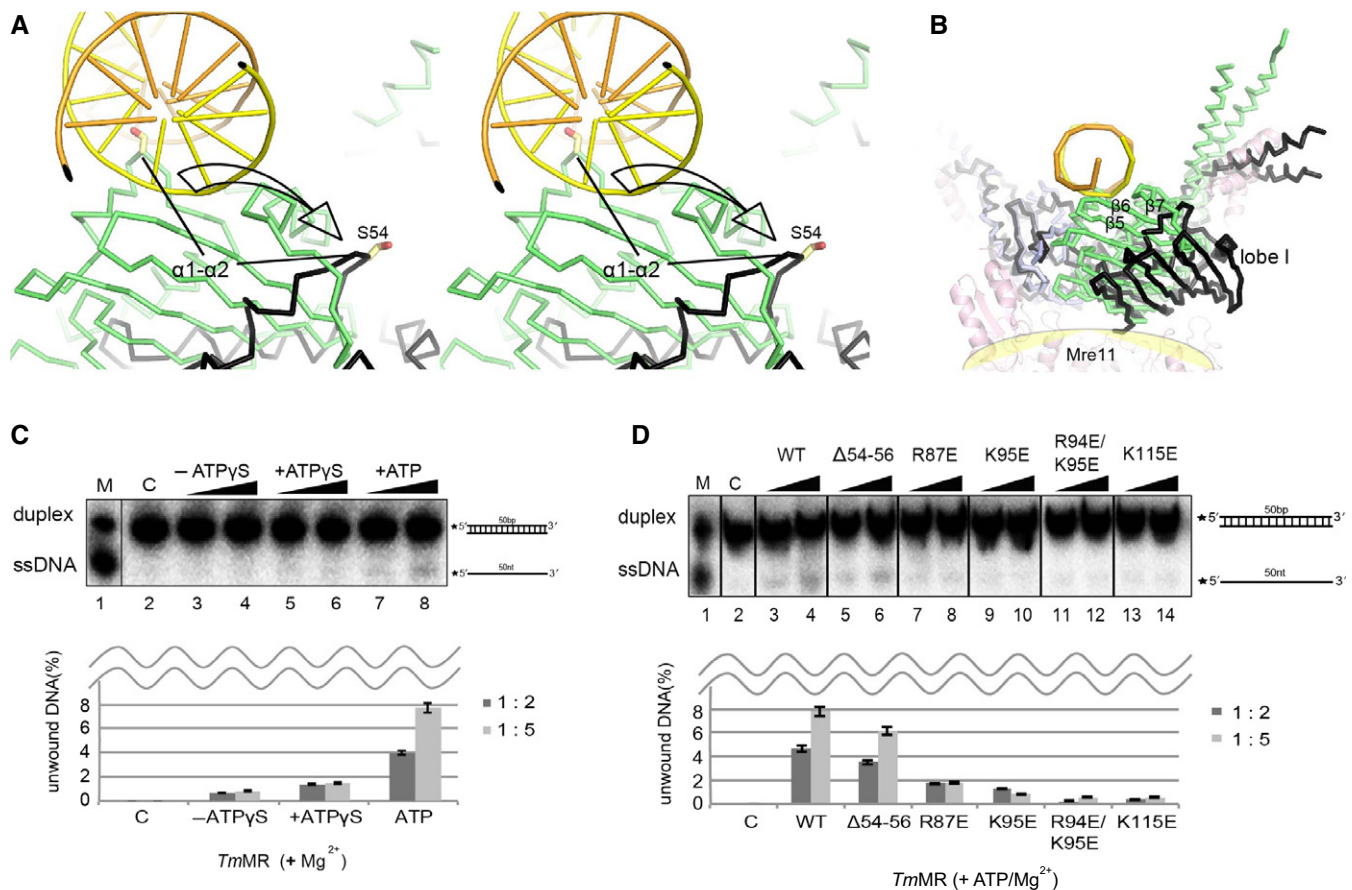
Figure 5. ATP-dependent DNA unwinding by the prokaryotic MR complex.

A   Stereo view of the superposition of the ADP–*Mj*Rad50 (3AUX) complex (black) onto the ATPγS–*Mj*MR–DNA complex (green) by aligning their lobe II domains. The α1-α2 loop that could collide with parts of the DNA molecule is indicated.

B   Aligning the lobe II domains of the two structures in (A) shows that rotation of the lobe I opens the gate for Mre11, which could allow the access of the unwound DNA. Color schemes are as in (A).

C   DNA unwinding activities of *Tm*MR. Lane 2, no protein; lanes 3 and 4, no ATP; lanes 5 and 6, with ATPγS; lanes 7 and 8, with ATP. The DNA:protein ratio was 1:2 for lanes 3, 5, and 7 and 1:5 for lanes 4, 6, and 8. A graph of the quantified data is shown in the lower panel. Plotted data represent the mean of three experiments, with error bars indicating one standard deviation.

D   Comparison of the ATP-dependent DNA unwinding activities of WT and mutant *Tm*MR proteins. Lane 2, no protein; lane 3 and 4, WT *Tm*MR; lane 5 and 6, Rad50 (Δ54–56) mutant; lane 7 and 8, R87E mutant; lane 9 and 10, K95E mutant; lane 11 and 12, R94E/K95E mutant; lane 13 and 14, K115E mutant. For each *Tm*MR, reaction contains 1:2 or 1:5 ratio of DNA: protein. Plotted data represent the mean of three experiments, with error bars indicating one standard deviation.

manner (Appendix Fig S4E). Based on the ATPγS–*Mj*MR–DNA structure, each wedge interacts with minor grooves, which are ~9–13 nt and 20–24 nt away from one end of the DNA, and this region of DNA is likely to be melted by the ATP hydrolysis-driven NBD rotation.

Puzzlingly, in six independent experiments using a fresh prepared protein sample, the *Tm*Rad50 K115E mutant repeatedly produced a 3-nt fragment as a major product. We do not know the biochemical basis of such activity but wondered if the altered binding of DNA to the MR complex by the mutation affects the hand-off process of a substrate, which may have incorrectly guided the phosphodiester bonds at the Mre11 active site. This unusual activity of the K115E mutant may lead to a reduced *in vivo* hairpin activity (Fig 6E, R131E variant) and increased sensitivity of *rad50*Δ *sgs1*Δ cells expressing the mutant toward damage-inducing drugs (see below, Appendix Fig S5).

DNA binding to Rad50 is important for DSB repair

We then determined whether DNA binding by Rad50 contributes to *in vivo* functions of the MRX complex in budding yeast. Centromeric plasmids expressing yeast rad50 variants with mutations at or near the DNA-binding surface (Δ55–57, R96E, K103E/K104E, R131E, see Fig 3A) were introduced into yeast cells deleted for *rad50* or *rad50 sgs1*. Yeasts were then subjected to DNA damage by treating cells with the indicated dose of camptothecin (CPT), methyl methanesulfonate (MMS), and phleomycin (PHL) whose repair depends on binding and resection of DNA ends by MRX complex. Considering severe deficiency of these mutants except Δ55–57 in DNA binding, we are surprised to find that most single *rad50* mutants except R96E and R131E showed near wild-type levels of resistance to genotoxic agent treatment (Figs 3A–E, 6D left panel, and EV3A–D, Appendix Fig S5 top panel). The results may reflect the limited
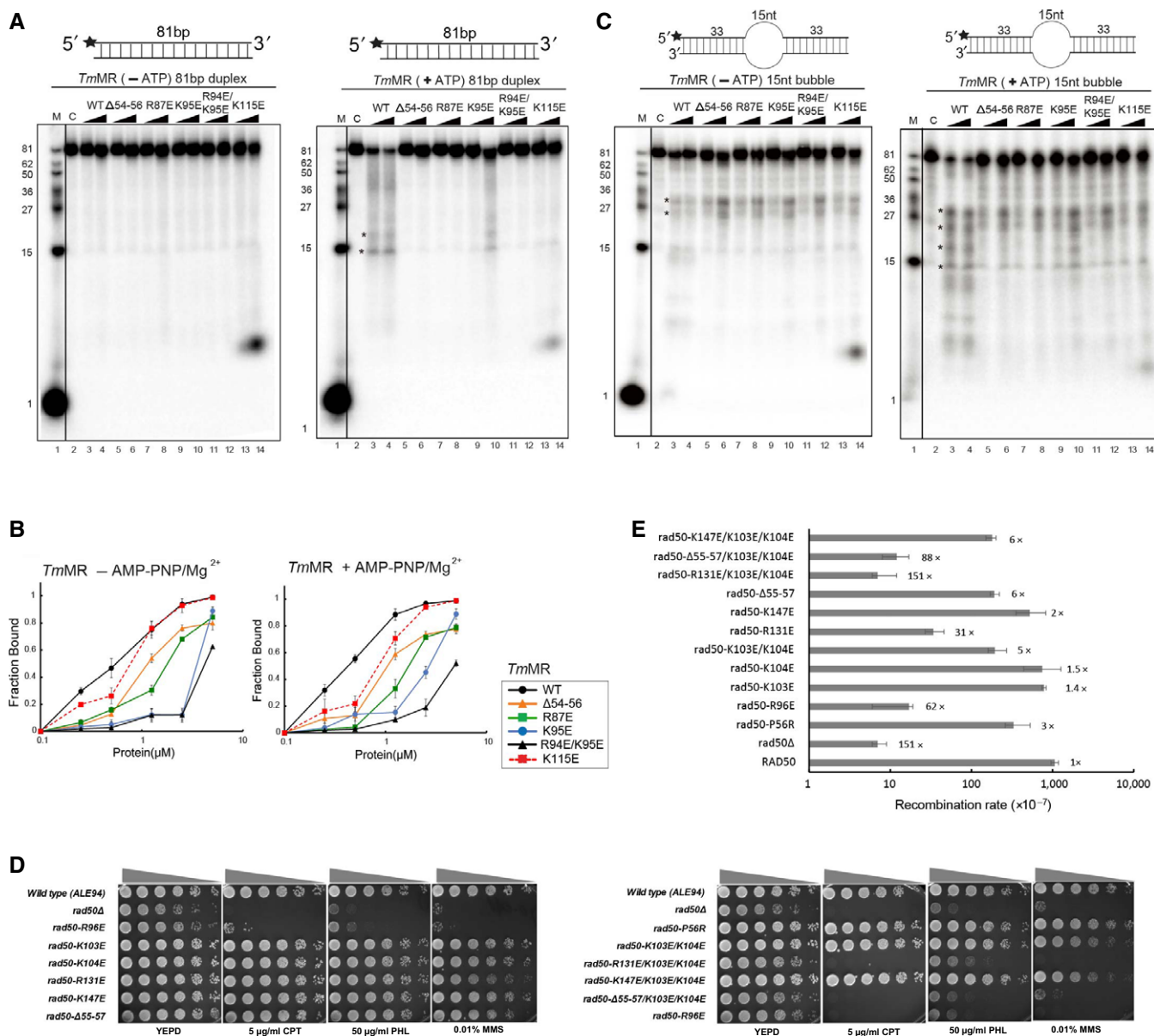
Figure 6. Effects of ATP-dependent binding of DNA to the MR complex.

A   Endonuclease activities of the *Tm*MR WT and mutant proteins toward a duplex DNA in the absence (left panel) or presence of ATP (right panel). Major products are marked with asterisks. The 5′-^{32}P-label is indicated by a star. See Appendix Fig S4A and B for the quantified values.

B   Quantification of a bubble DNA binding by WT or mutant *Tm*MR in the presence or absence of AMP-PNP. See Appendix Fig S3E and F for the original data. Plotted data represent the mean of three experiments, with error bars indicating one standard deviation.

C   Endonuclease activities of the WT and mutant *Tm*MR proteins toward a bubble DNA molecule in the absence (left panel) or presence of ATP (right panel). See Appendix Fig S4C and D for the quantified values. Major products are marked with asterisks.

D   The effects of single or multiple point mutations in the DNA-contacting or neighboring residues of *Saccharomyces cerevisiae* rad50 on the sensitivity to chemical drugs. Sensitivities of *rad50Δ* expressing the mutants toward indicated concentrations of CPT, PHL, and MMS were examined.

E   The effects of *rad50* mutation on recombination stimulated by inverted *Alu* repeats. Shown is the mean of two independent experiments. See Table EV1 for the quantified values.

conservation of the DNA-contacting residues of Rad50 proteins between prokaryotic MR and yeast MRX complexes. Alternatively, the results could be due to the limitations of *in vitro* DNA binding and endonuclease assay and/or additional factors related to *in vivo* environment. In this scenario, a single-site mutation might not be

sufficient to disrupt *in vivo* DNA binding by Rad50 due to clustering of weak binding contacts. We thus combined each mutation to generate double or triple rad50 mutants and assessed their sensitivities from *rad50Δ* or *rad50Δ sgs1Δ* cells that express the rad50 mutants upon genotoxic agent treatment. We then found that the

rad50 bearing Δ55-57/K103E/K104E or K103E/K104E/R131E mutation conferred a severe sensitivity to all three drugs in *rad50* or both *rad50 sgs1* deleted cells (Fig 6D right panel, Appendix Fig S5 bottom panel). Notably, all rad50 variants were expressed at levels almost indistinguishable from that of WT Rad50, with exception of R96E, which showed the significant reduction in rad50 level (Appendix Fig S6). All the mutant proteins except R96E mutant also sustain the integrity of MRX complex, suggesting that multi-site mutations did not compromise the stability and gross structural properties of the complex (Appendix Fig S7). Thus, unlike the prokaryotic R86E variant that forms a stable Mre11/Rad50 complex, the severe drug sensitivity of *rad50-R96E* in yeast likely stems from an inability to produce stable complex, which is known to be essential for all functions associated with MRX complex.

To further investigate the effect of the *rad50* mutations on endonuclease activity of MRX *in vivo*, we measured the rate of recombination between *Alu* repeats from *S. cerevisiae* harboring these mutations (Lobachev *et al*, 2002). To this end, we engineered *rad50* mutations into its own genomic locus in yeast strains carrying inverted *Alu* repeats at *lys2* locus and monitored the frequency of recombination by scoring LYS$^+$ revertants. Three *rad50* mutants, Δ55–57, R131E, and K103E/K104, exhibited moderately decreased *lys2* reversion frequency, whereas *rad50 R96E* mutant exhibited a near null level of *lys2* revertant formation (Fig 6E, Table EV1). When single mutations were combined, the effects became more pronounced such that two multi-site mutants (Δ55–57/K103E/K104E and R131E/K103E/K104E) exhibited severe recombination defects. By contrast, the K147E/K103E/K104E mutant that is resistant to damage-inducing drugs exhibited recombination efficiency similar to that of wild-type *RAD50*. These results mirror that of the cell survival assay toward CPT, which suggests that the sensitivity toward CPT is tightly correlated with *in vivo* endonuclease activity of the MRX complex in the yeast strain. Collectively, these results support the premise that DNA binding activity of Rad50 is critical for endonuclease activity of MRX *in vivo* even though yeast can readily tolerate a single-site mutation at the interface of Rad50 and the multiple-site mutations is needed to express its effect.

Discussion

Damaged DNA recognition by the MRN/X complex is the central feature of the early DSB repair events. The MRN complex can bind to DNA in either the absence or the presence of ATP (Alani *et al*, 1990; Hopfner *et al*, 2000a,b; Bhaskara *et al*, 2007; Lee *et al*, 2013). However, a number of studies showed that the ATP-induced NBD dimer formation is important for the functional DNA binding by Rad50. Yet, the underlying biochemistry and molecular biology of ATP-dependent DNA binding and how it plays critical roles in DNA unwinding, stimulation of the endonuclease activities, end joining, and ATM kinase activation by the MRN (or MRX) complex are still elusive (Alani *et al*, 1990; Hopfner *et al*, 2000a,b; Lee *et al*, 2003; Cannon *et al*, 2013; Deshpande *et al*, 2014). Recently, Rojowska *et al* reported crystal structure of the DNA-bound MR complex in the presence of AMP-PNP (2014). In the structure, the DNA molecule binds to only one of the two NBDs of the MR complex despite ATP-induced NBD dimer formation is essential for DNA binding. Thus, it remains unclear how ATP binding to the MR complex

promotes diverse ATP-dependent functions of the complex. Mutational studies revealed that functionally critical DNA-contacting residues are located at the central groove, which is distant from the DNA-binding site in the reported structure, suggesting that additional DNA binding site is likely present in the NBDs of Rad50 dimer (Lim *et al*, 2011; Rojowska *et al*, 2014).

In the present study, we showed that an ATPγS-bound tetrameric MR complex recognizes the duplex DNA via a positively charged surface at the central groove between two Rad50 NBDs that forms only in the presence of ATP or ATPγS. This structural feature explains why ATP is required for the functional DNA binding by Rad50 (Alani *et al*, 1990; Raymond & Kleckner, 1993; Hopfner *et al*, 2000a,b). DNA binding by ATPγS-bound Rad50 NBDs is clearly distinguishable from that by SMC proteins such as cohesin and condensin that interact with DNA via their hinge domain despite the fact that all members of this family share similar ATPase head domain structures (Hirano, 2006). Presumably, ATP-dependent DNA binding property of the NBD of Rad50 has evolved to perform unique function in tethering, signaling, and resecting of DNA ends.

Previous structural studies using the coiled-coil deleted prokaryotic MRcd complex showed that the nucleotide-free MR complex forms an open head conformation, whereas the nucleotide-bound MR complex forms a closed head structure, where the active site of Mre11 is blocked by Rad50 dimer (Lammens *et al*, 2011; Lim *et al*, 2011; Möckel *et al*, 2012). Indeed, our EMSA and nuclease activity analyses (Fig 3B and C) reconfirm these structural findings. Surprisingly, the nucleotide-free full-length MR complex exhibited DNA binding and cleavage patterns different from that of the nucleotide-free coiled-coil deleted MRcd (Figs 3D–G and EV3C and D). Although we do not exclude a possibility that the observed DNA binding and cleavage differences between the full-length and the coiled-coil deleted MR complexes might reflect different temperature optima for the archaeal versus eubacterial thermophilic enzymes or the limited conservation between these two complexes, we interpret the data that the presence of the coiled-coils and a zinc hook in full-length MR might impose restraints on the ATP-free Rad50 head domains. Recent studies showed that zinc-hook and head domains interdependently regulate each other via coiled-coil arms in yeast MRX (Hohl *et al*, 2015). The coiled-coil and hook domains are important for a myriad of the globular domain function of MRX including end joining, resection, telomere maintenance, Tel1 activation, and assembly of the MRX complex (Hopfner *et al*, 2002; Hohl *et al*, 2011, 2015; Barfoot *et al*, 2015). We propose that the two NBDs are located closely together in the nucleotide-free full-length MR complex, which could prevent the access of DNA to Mre11. Consistent with this model, Nbs1, which binds to the closed state of human MR, but not the open state, interacts efficiently with the ATP-free intact human MR complex (Lee *et al*, 2013). Furthermore, cross-linking analyses of the archaeal full-length Rad50 head domain showed that two NBDs can be linked by hydrogen peroxide in the ATP-free state, suggesting that two head domains are arranged in close proximity (Deshpande *et al*, 2014). ATP binding and hydrolysis by the archaeal full-length MR and MRcd complexes were shown significantly different (Deshpande *et al*, 2014). Nelson and co-workers suggested that an ATP-free open state is unlikely present in the full-length phage T4 MR complex (Barfoot *et al*, 2015).

Symmetrical binding of DNA to the central groove of an ATP-bound Rad50 dimer provides several insights into understanding the
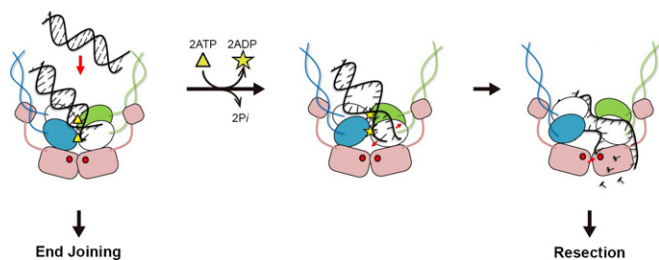
Figure 7. A model for the ATP-dependent DNA binding, melting, and endonuclease activities of the MR complex.
Initial recognition of DNA by ATP-bound MR results in partial deformation of the DNA. ATP hydrolysis induces a lobe rotation of Rad50 NBDs that melts both the internal segment and ends of the DNA, which subsequently access the Mre11 active site.

functions of the MR complex. First, positioning of the DNA molecule on top of the two ATP-bound NBDs could allow Rad50 to melt the DNA at least partially via ATP hydrolysis-driven lobe rotation (Figs 5A and C, and 7, Paull & Gellert, 1999). Upon ATP hydrolysis, the α1-α2 loop of Rad50 undergoes positional alteration, and during this process, the α1-α2 loop from each Rad50 could collide with phosphate backbone residues at minor groove and disrupt its structure, which may explain the ATP-dependent DNA melting activity by the MR complex (Fig 5A, Movie EV3). Second, the rotated lobes of Rad50 can generate a space, through which ssDNA but not dsDNA passes to access Mre11 in the MR complex (Figs 5B and 7). This model might explain the similar dsDNA-binding patterns by the nucleotide-free and nucleotide-bound intact MR complexes, and impaired endonuclease activities toward dsDNA by the nucleotide-free intact MR complex (Fig 3B–G). Consistently, the bubble DNA, but not intact dsDNA, was cleaved by the ATP-free MR mutants, and the bubble DNA bound more efficiently to the ATP-free MR complex than intact dsDNA (Fig 6A–C). The model we propose may provide a basis for the observation that the presence of ATP and Rad50 stimulates the endonuclease activity of Mre11, although Mre11 dimer alone can cleave hairpin DNA (Fig 3F and G; Williams *et al*, 2008; Sung *et al*, 2014).

Previous *Tm*MR-DNA and current *Mj*MR-DNA structures demonstrated that the MR complex recognizes DNA region distant from the end. It thus remains unclear how the MR complex recognizes DNA end and catalyzes ATM-dependent signaling. In the end blocked DNA, the MRX complex is preferably bound to a site which is ~15–25 nt away from the 5′ blocked end and makes an endonucleolytic incision (Cannavo & Cejka, 2014; Shibata *et al*, 2014). Symmetrical DNA binding by the M2R2 tetramer requires two minor grooves, in which each minor groove is recognized by three motifs of each Rad50 molecule (Fig 2A, B and E). Such structure-specific recognition by Rad50 may explain DNA binding at the internal site by the MR complex. We do not rule out the possibility that the MR complex binds to the internal region and slides along the DNA to sense the minor groove near the terminal end. The MR complex might recognize DNA ends by inducing Rad50-dependent DNA deformation from the ideal B-form DNA conformation. DNA deformation then could trigger ATM activation signaling and assembly of end-joining complex at the DNA ends (Lee & Paull, 2005; Lee *et al*, 2013). Given that the conformations of the ATP-free and ATP-bound MR complexes play important roles in determining the DSB repair pathway (Deshpande *et al*, 2014), the

conformational change of MR and the associated DNA could dictate the repair pathway choice. Further studies are required to understand whether the DNA conformation would play a crucial role in sensing, end joining, and resection by the MR complex.

Materials and Methods

Protein expression and purification for the *Mj*MRcd complex

The *Mj*MR complex was produced by co-expressing the two proteins from *Escherichia coli* Rosetta (DE3), as described previously (Lim *et al*, 2011). Briefly, cDNAs encoding residues 1–190 and residues 825–1,005 of *Mj*Rad50 were inserted into pCDFDuet-1 and pETDuet-1, respectively, and *Mj*Mre11 (residues 1–366) was inserted into the pET28a vector. The complex was first purified by Ni-NTA affinity chromatography. The *Mj*MR complex was subsequently eluted with 300 mM imidazole in the same buffer. Fractions containing the *Mj*MR complex were purified using cation exchange (Resource S) and gel-filtration chromatography (Superdex 200), and concentrated by ultrafiltration. All *Mj*MR mutant proteins were purified by the same procedure.

For the full-length *Tm*MR complex, the cDNAs encoding full-length *Tm*Mre11 and *Tm*Rad50 were inserted into pET28a and pCDFDuet-1, respectively, and co-expressed in *Escherichia coli* Rosetta (DE3). The full-length WT or mutant *Tm*MR complex was purified by Ni-NTA affinity chromatography, anion exchange (Hi-trap Q), and gel-filtration chromatography (Superdex 200).

Crystallization and data collection

Crystals of the ATPγS–*Mj*MR complex bound to DNA were grown at 18°C by the hanging-drop vapor diffusion method. The crystallization buffer contained 24% PEG 400, 0.1 M Tris–HCl (pH 8.0), 1 mM ATPγS, 0.1 mM MgCl$_2$, and 0.1 M trimethylamine hydrochloride. A 25-bp duplex DNA with a 2-nt 5′ overhang at each end was used for crystallization. The ATPγS–*Mj*MR-DNA crystals formed in the space group P2$_1$2$_1$2$_1$ (a = 84.3 Å, b = 130.1 Å, and c = 166.6 Å) and contained two ATPγS–*Mj*MR complexes and one DNA molecule in the asymmetric unit. Diffraction data were collected at −170°C using crystals flash-frozen in crystallization buffer containing 30% (v/v) glycerol. Diffraction data were collected at 0.9795 Å on Beamline 5C at the Pohang Accelerator Laboratory. Diffraction data were integrated and scaled using the HKL2000 package (Otwinowski & Minor, 1997).

To improve the usable resolution and quality of the resulting electron density maps, we used the Karplus CC* (Pearson correlation coefficient)-based data cutoff approach (Table 1; Karplus & Diederichs, 2012, 2015). We took into account following criteria to improve the resolution limit: (i) CC$_{1/2}$ > ~40% based on data merging statistics, (ii) a Karplus CC* analysis against unmerged intensities in the Phenix package (higher CC* relative to CC$_{work}$ and CC$_{free}$) to avoid overfitting, and (iii) R$_{free}$ of the highest resolution shell against the refined structure being < ~40% (Appendix Fig S1A).

Structure determination and refinement

The structure of the ATPγS–*Mj*MR–DNA complex was determined by the molecular replacement method. The *Mj*Rad50 molecules

were located with the PHASER program, followed by a search for *Mj*Mre11 (McCoy *et al*, 2007; Lim *et al*, 2011; Sung *et al*, 2014). After density modification, an electron density map was generated at a resolution of 3.1 Å using the PHENIX program (Adams *et al*, 2010); the map was of good quality and revealed most DNA chains. Successive rounds of model building using COOT (Emsley & Cowtan, 2004) and refinement using PHENIX (using rigid body, xyz coordinates, individual B-factor, NCS, and TLS refinements) were performed to build the complete model. The final refined model of the ATPγS–*Mj*MR–DNA complex at 3.1 Å (R_{work}/R_{free} = 22.2/26.9%) contains 92.9% of residues in the most favored region and no residue in the disallowed region (Table 1).

DNA binding assays

For the DNA binding analysis, *Mj*MRcd or *Tm*MR proteins were incubated with a closed circular dsDNA molecule (φX174 RFII; NEB), a linear dsDNA (EcoRI-treated pCDFDuet-1), or a bubble DNA in 20 μl reactions containing reaction buffer (25 mM Tris–HCl, pH 7.4, 50 mM NaCl, 5 mM β-mercaptoethanol, and 5% glycerol) in the absence or presence of 1 mM AMP-PNP and 5 mM MgCl$_2$. For DNA binding analysis, each protein sample was incubated with φX174 RFII or a linear dsDNA (3.5 nM; the molar ratio of protein: DNA was 50:1, 100:1, 200:1, 500:1, 1,000:1, or 2,000:1) for 30 min at 4°C. After mixing with 6× loading dye [0.4% orange G, 0.03% bromophenol blue, 0.03% xylene cyanol FF, 15% Ficoll 400, 10 mM Tris–HCl (pH 7.5)], the samples were resolved by electrophoresis (100 V for 20 min) through a 0.5% agarose gel in 0.5× TB buffer and visualized by ethidium bromide staining. For the bubble DNA binding analysis, a 15-nt bubble DNA (2.5 nM) was incubated with various amount of *Mj*MRcd or *Tm*MR proteins at 4°C for 30 min. The molar ratio of protein: DNA was 100:1, 200:1, 500:1, 1,000:1, or 2,000:1. The reaction mixture was resolved by 6% native polyacrylamide gel electrophoresis.

DNA unwinding assays

DNA unwinding reaction mixtures (20 μl) contained 2.5 nM of ^{32}P-labeled DNA substrate and *Tm*MR mutant proteins (5 or 12.5 nM) in reaction buffer (25 mM HEPES, pH 7.4, 25 mM NaCl, 5 mM β-mercaptoethanol, 4% glycerol, 50 nM MgCl$_2$, and 0.1 mM ATP). The reactions were incubated at 25°C for 15 min and then stopped by the addition of EDTA and SDS to final concentrations of 5 mM and 0.3%, respectively. The helicase reaction products were analyzed by polyacrylamide gel electrophoresis using non-denaturing 15% polyacrylamide gels and were separated for approximately 90 min at 100 V. The intensity of the unwound substrate bands was analyzed by ImageQuant TL (Amersham Biosciences).

Nuclease assays

The reaction mixture (20 μl) contained 10 nM DNA substrate and 100 or 200 nM *Tm*MR (or *Mj*MRcd) in reaction buffer (25 mM HEPES, pH 7.4, 5 mM β-mercaptoethanol, 50 mM NaCl, and 5% glycerol) containing 5 mM MnCl$_2$, 1 mM MgCl$_2$, and 1 mM ATP (or no ATP). The reaction mixture was incubated for 30 min at 55°C (or

for 15 min at 25°C) and stopped by adding the same volume of 2× reaction stop buffer (95% formamide, 18 mM EDTA, 0.025% SDS, and 0.01% bromophenol blue), followed by 5 min of boiling at 100°C. The products were resolved on 15% denaturing polyacrylamide gels containing 7 M urea in 1× Tris–borate–EDTA for 120 min at 13 Vcm^{-1}. The intensities of the uncleaved substrate bands were quantitated using a phosphorimager. All assays were repeated at least three times.

ATP hydrolysis assay

ATP hydrolysis activity was quantified by the BIOMOL GREEN assay (BIOMOL Research Labs, Inc.) using 1 mM ATP and various concentrations of MR proteins (200, 400, 800 nM). The mixtures were incubated at 37 or 55°C (*Mj*MRcd or *Tm*MR, respectively) for 20 min in buffer containing 25 mM Tris–HCl (pH 7.5), 50 mM NaCl, 5 mM MgCl$_2$, and 1 mM DTT and were subsequently incubated on ice. A suitable amount of BIOMOL GREEN reagent was added to the mixtures, which were incubated for 20 min at 25°C and then measured at OD$_{620}$. The amounts of released free phosphate in the mixtures were determined by subtracting the background phosphate.

Mutagenesis

All of the mutants used in this study were constructed by PCR-based methods (Stratagene). For the *Mj*Rad50 mutants, residues 53–55 were deleted, or Arg86, Arg92, or Thr107 was mutated to glutamic acid. For the *Tm*Rad50 mutants, residues 54–56 were deleted, or Arg87, Lys95, or Lys115 was mutated to glutamic acid; Arg94 and Lys95 were simultaneously mutated to glutamic acid. For the *Tm*Mre11 nuclease-inactive mutant, His94 was mutated to serine. For the *Sc*Rad50 mutants, residues 55–57 were deleted; Arg96, Lys103, Lys104, or Arg131 was mutated to glutamic acid; or Lys103 and Lys104 were simultaneously mutated to glutamic acid.

Recombination rate determination

This assay follows typical fluctuation test described in Lobachev *et al* (2002) with minor modification. Briefly, 500–1,000 yeast cells were inoculated in YEPD and cultured for 3 days. Cells were diluted and plated onto Lysine dropout plate, to monitor the LYS$^+$ recombination event, and YEPD plate to monitor the input cell number, respectively. After 3 days culture in 30°C incubator, colonies were counted. At least 12 independent colonies from two isolates were scored to calculate recombination rate and 95% confidence intervals as described (Spell & Jinks-Robertson, 2004).

Drug sensitivity assay

Yeast cells expressing WT Rad50, Rad50 variants with different mutations, or *rad50* gene deleted were cultured in YEPD media for 32–72 h until they reached a density of approximately 4×10^7 cells/ml. Subsequently, approximately 2×10^6 cells were transferred into 200 μl of sterilized distilled water and subjected to 1:5 serial dilutions. Cells at different densities were spotted onto YEPD agar plates containing the indicated concentrations of camptothecin, phleomycin, or methyl methanesulfonate and incubated at 30°C for 48–72 h.

Yeast genetic analyses

The yeast strains used in this study are derivatives of SLY1A (*ho*Δ *hml::ADE1 MAT*α *hml::ADE1 ade1 leu2-3,112 lys5 trp1::hisG ura3-52 ade3::GAL10::HO*) or ALE94. All single gene deletions or replacements were performed using a PCR-derived selection gene product flanked by short terminal sequences homologous to the ends of each gene's open reading frame, or to the sequence flanking the region to be replaced (Li *et al*, 2013). *Saccharomyces cerevisiae* strain ALE94 (*MAT*α, *ade5-1*, *his7-2*, *leu2-3,112*:: *p305L3 (LEU2)*, *trp1-289*, *ura3-*Δ, *lys2::AluIR*) was utilized to monitor the recombination event stimulated by inverted *Alu* repeats. *rad50* mutations were introduced into genomic locus and confirmed by sequencing. More than two independent isolates with each mutation were utilized for subsequent genetic analysis.

Western blot analysis

Trichloroacetate (TCA)-precipitated *S. cerevisiae* lysates were prepared as described before (Yaffe & Schatz, 1984) with modification: *S. cerevisiae* were grown to A_{600} of 1.0 in plasmid-maintaining liquid media at 30°C. Cells were harvested and lysed with 1 ml 0.2 M NaOH, 1% β-mercaptoethanol. Total protein was precipitated by additional 10% TCA. Protein pellet was re-suspended in 50 μl SDS–PAGE sample buffer. For analysis, 20 μl of each sample was separated by 8% SDS–polyacrylamide gel and transferred onto nitrocellulose membrane, followed by immunoblotting with anti-rad50 and anti-tubulin antibodies. Antibodies against *S. cerevisiae* Rad50 were a kind gift of Dr. John Petrini.

Yeast two-hybrid assay

Yeast two-hybrid system analysis was performed with a GAL4 DNA-binding domain (BD)-fused Mre11 and a GAL4 activation domain (AD)-fused Rad50. The bait (BD-Mre11) and the prey (AD-Rad50) proteins were co-expressed in the yeast strain PBN204 (*MATa, pGAL1-lacZ, pGAL1-URA3, pGAL2-ADE2, trp1-901, leu2-3, gal4*Δ, *gal80*Δ). PBN204 contains *URA3*, *ADE2*, and beta-galactosidase as reporter genes and *trp1* and *leu2* as selection marker genes (Panbionet Inc.). Co-transformation of BD-polypyrimidine tract-binding protein (PTB) and AD-PTB served as a positive control for the protein–protein interaction. PTB is a homo-dimeric protein. Plasmids pGBKT7 and pGADT7 were used as a negative control.

Expanded View for this article is available online.

Author contributions

YL carried out crystallization and structure determination with the help of YK and GHG; YL, FL, SS, AJ, TK, and GHG participated in biochemical experimental design and data analysis; FL and S-EL designed and performed yeast genetics experiment; A-KK and O-KS performed yeast two-hybrid experiment; YC and S-EL conceived of the project and wrote the paper.

Conflict of interest

The authors declare that they have no conflict of interest.

References

Adams PD, Afonine PV, Bunkóczi G, Chen VB, Davis IW, Echols N, Headd JJ, Hung LW, Kapral GJ, Grosse-Kunstleve RW, McCoy AJ, Moriarty NW, Oeffner R, Read RJ, Richardson DC, Richardson JS, Terwilliger TC, Zwart PH (2010) PHENIX: a comprehensive Python-based system for macromolecular structure solution. *Acta Crystallogr D* 66: 213–221

Alani E, Padmore R, Kleckner N (1990) Analysis of wild-type and rad50 mutants of yeast suggests an intimate relationship between meiotic chromosome synapsis and recombination. *Cell* 61: 419–436

Barfoot T, Herdendorf TJ, Behning BR, Stohr BA, Gao Y, Kreuzer KN, Nelson SW (2015) Functional analysis of the bacteriophage T4 Rad50 homolog (gp46) coiled-coil domain. *J Biol Chem* 290: 23905–23915

Bhaskara V, Dupré A, Lengsfeld B, Hopkins BB, Chan A, Lee JH, Zhang X, Gautier J, Zakian V, Paull TT (2007) Rad50 adenylate kinase activity regulates DNA tethering by Mre11/Rad50 complexes. *Mol Cell* 25: 647–661

Boulton SJ, Jackson SP (1998) Components of the Ku-dependent nonhomologous end-joining pathway are involved in telomeric length maintenance and telomeric silencing. *EMBO J* 17: 1819–1828

Buis J, Wu Y, Deng Y, Leddon J, Westfield G, Eckersdorff M, Sekiguchi JM, Chang S, Ferguson DO (2008) Mre11 nuclease activity has essential roles in DNA repair and genomic stability distinct from ATM activation. *Cell* 135: 85–96

Cannavo E, Cejka P (2014) Sae2 promotes dsDNA endonuclease activity within Mre11-Rad50-Xrs2 to resect DNA breaks. *Nature* 514: 122–125

Cannon B, Kuhnlein J, Yang SH, Cheng A, Schindler D, Stark JM, Russell R, Paull TT (2013) Visualization of local DNA unwinding by Mre11/Rad50/Nbs1 using single-molecule FRET. *Proc Natl Acad Sci USA* 110: 18868–18873

Cejka P, Cannavo E, Polaczek P, Masuda-Sasa T, Pokharel S, Campbell JL, Kowalczykowski SC (2010) DNA end resection by Dna2-Sgs1-RPA and its stimulation by Top3-Rmi1 and Mre11-Rad50-Xrs2. *Nature* 467: 112–116

Chen L, Trujillo KM, Van Komen S, Roh DH, Krejci L, Lewis LK, Resnick MA, Sung P, Tomkinson AE (2005) Effect of amino acid substitutions in the rad50 ATP binding domain on DNA double strand break repair in yeast. *J Biol Chem* 280: 2620–2627

Chen VB, Arendall WB III, Headd JJ, Keedy DA, Immormino RM, Kapral GJ, Murray LW, Richardson JS, Richardson DC (2010) MolProbity: all-atom structure validation for macromolecular crystallography. *Acta Crystallogr D Biol Crystallogr* 66: 12–21

Connelly JC, de Leau ES, Okely EA, Leach DR (1997) Overexpression, purification, and characterization of the SbcCD protein from *Escherichia coli*. *J Biol Chem* 272: 19819–19826

Darmon E, Eykelenboom JK, Lincker F, Jones LH, White M, Okely E, Blackwood JK, Leach DR (2010) *Escherichia coli* SbcCD and RecA control chromosomal rearrangement induced by an interrupted palindrome. *Mol Cell* 39: 59–70

Deshpande RA, Williams GJ, Limbo O, Williams RS, Kuhnlein J, Lee JH, Classen S, Guenther G, Russell P, Tainer JA, Paull TT (2014) ATP-driven Rad50

conformations regulate DNA tethering, end resection, and ATM checkpoint signaling. *EMBO J* 33: 482–500

Emsley P, Cowtan K (2004) Coot: model-building tools for molecular graphics. *Acta Crystallogr D Biol Crystallogr* 60: 2126–2132

Furuse M, Nagase Y, Tsubouchi H, Murakami-Murofushi K, Shibata T, Ohta K (1998) Distinct roles of two separable *in vitro* activities of yeast Mre11 in mitotic and meiotic recombination. *EMBO J* 17: 6412–6425

Garcia V, Phelps SEL, Gray S, Neale MJ (2011) Bidirectional resection of DNA double-strand breaks by Mre11 and Exo1. *Nature* 479: 241–244

Hirano T (2006) At the heart of the chromosome: SMC proteins in action. *Nat Rev Mol Cell Biol* 7: 311–322

Hohl M, Kwon Y, Galván SM, Xue X, Tous C, Aguilera A, Sung P, Petrini JH (2011) The Rad50 coiled-coil domain is indispensable for Mre11 complex functions. *Nat Struct Mol Biol* 18: 1124–1131

Hohl M, Kochańczyk T, Tous C, Aguilera A, Krężel A, Petrini JH (2015) Interdependence of the rad50 hook and globular domain functions. *Mol Cell* 57: 479–491

Hopfner KP, Karcher A, Shin DS, Craig L, Arthur LM, Carney JP, Tainer JA (2000a) Structural biology of Rad50 ATPase, ATP-driven conformational control in DNA double-strand break repair and the ABC-ATPase superfamily. *Cell* 101: 789–800

Hopfner KP, Karcher A, Shin D, Fairley C, Tainer JA, Carney JP (2000b) Mre11 and Rad50 from *Pyrococcus furiosus*, cloning and biochemical characterization reveal an evolutionarily conserved multiprotein machine. *J Bacteriol* 182: 6036–6041

Hopfner KP, Karcher A, Craig L, Woo TT, Carney JP, Tainer JA (2001) Structural biochemistry and interaction architecture of the DNA double-strand break repair Mre11 nuclease and Rad50-ATPase. *Cell* 105: 473–485

Hopfner KP, Craig L, Moncalian G, Zinkel RA, Usui T, Owen BA, Karcher A, Henderson B, Bodmer JL, McMurray CT, Carney JP, Petrini JH, Tainer JA (2002) The Rad50 zinc-hook is a structure joining Mre11 complexes in DNA recombination and repair. *Nature* 418: 562–566

de Jager M, van Noort J, van Gent DC, Dekker C, Kanaar R, Wyman C (2001) Human Rad50/Mre11 is a flexible complex that can tether DNA ends. *Mol Cell* 8: 1129–1135

Karplus PA, Diederichs K (2012) Linking crystallographic model and data quality. *Science* 336: 1030–1033

Karplus PA, Diederichs K (2015) Assessing and maximizing data quality in macromolecular crystallography. *Curr Opin Struct Biol* 34: 60–68

Lafrance-Vanasse J, Williams GJ, Tainer JA (2015) Envisioning the dynamics and flexibility of Mre11-Rad50-Nbs1 complex to decipher its roles in DNA replication and repair. *Prog Biophys Mol Biol* 117: 182–193

Lammens K, Bemeleit DJ, Möckel C, Clausing E, Schele A, Hartung S, Schiller CB, Lucas M, Angermüller C, Söding J, Strässer K, Hopfner KP (2011) The Mre11, Rad50 structure shows an ATP-dependent molecular clamp in DNA double-strand break repair. *Cell* 145: 54–66

Larkin MA, Blackshields G, Brown NP, Chenna R, McGettigan PA, McWilliam H, Valentin F, Wallace IM, Wilm A, Lopez R, Thompson JD, Gibson TJ, Higgins DG (2007) Clustal W and clustal X version 2.0. *Bioinformatics* 23: 2947–2948

Lee JH, Ghirlando R, Bhaskara V, Hoffmeyer MR, Gu J, Paull TT (2003) Regulation of Mre11/Rad50 by Nbs1: effects on nucleotide-dependent DNA binding and association with ATLD mutant complexes. *J Biol Chem* 278: 45171–45181

Lee JH, Paull TT (2005) ATM activation by DNA double-strand breaks through the Mre11-Rad50-Nbs1 complex. *Science* 308: 551–554

Lee JH, Mand MR, Deshpande RA, Kinoshita E, Yang SH, Wyman C, Paull TT (2013) Ataxia telangiectasia-mutated (ATM) kinase activity is regulated by

ATP-driven conformational changes in the Mre11/Rad50/Nbs1 (MRN) complex. *J Biol Chem* 288: 12840–12851

Li F, Dong JC, Eichmiller R, Holland C, Minca E, Prakash R, Sung P, Shim EY, Surtees JA, Lee SE (2013) Role of Saw1 in Rad1/Rad10 complex assembly at recombination intermediates in budding yeast. *EMBO J* 32: 461–472

Lim HS, Kim JS, Park YB, Gwon GH, Cho YJ (2011) Crystal structure of the Mre11-Rad50-ATPγS complex: understanding the interplay between Mre11 and Rad50. *Genes Dev* 25: 1091–1104

Limbo O, Chahwan C, Yamada Y, de Bruin RA, Wittenberg C, Russell P (2007) Ctp1 is a cell-cycle-regulated protein that functions with Mre11 complex to control double-strand break repair by homologous recombination. *Mol Cell* 28: 134–146

Liu C, Pouliot JJ, Nash HA (2002) Repair of topoisomerase I covalent complexes in the absence of the tyrosyl-DNA phosphodiesterase Tdp1. *Proc Natl Acad Sci USA* 99: 14970–14975

Lobachev KS, Gordenin DA, Resnick MA (2002) The Mre11 complex is required for repair of hairpin-capped double-strand breaks and prevention of chromosome rearrangements. *Cell* 108: 183–193

McCoy AJ, Grosse-Kunstleve RW, Adams PD, Winn MD, Storoni LC, Read RJ (2007) Phaser crystallographic software. *J Appl Cryst* 40: 658–674

Mimitou EP, Symington LS (2008) Sae2, Exo1 and Sgs1 collaborate in DNA double-strand break processing. *Nature* 455: 770–774

Möckel C, Lammens K, Schele A, Hopfner KP (2012) ATP driven structural changes of the bacterial Mre11:Rad50 catalytic head complex. *Nucleic Acids Res* 40: 914–927

Moreau S, Ferguson JR, Symington LS (1999) The nuclease activity of Mre11 is required for meiosis but not for mating type switching, end joining, or telomere maintenance. *Mol Cell Biol* 19: 556–566

Moreno-Herrero F, de Jager M, Dekker NH, Kanaar R, Wyman C, Dekker C (2005) Mesoscale conformational changes in the DNA-repair complex Rad50/Mre11/Nbs1 upon binding DNA. *Nature* 437: 440–443

Neale MJ, Pan J, Keeney S (2005) Endonucleolytic processing of covalent protein-linked DNA double-strand breaks. *Nature* 436: 1053–1057

Otwinowski Z, Minor W (1997) Processing of X-ray diffraction data collected in oscillation mode. *Methods Enzymol* 276: 307–326

Park YB, Chae J, Kim YC, Cho Y (2011) Crystal structure of human Mre11: understanding tumorigenic mutations. *Structure* 19: 1591–1602

Paull TT, Gellert M (1998) The 3′ to 5′ exonuclease activity of Mre 11 facilitates repair of DNA double-strand breaks. *Mol Cell* 1: 969–979

Paull TT, Gellert M (1999) Nbs1 potentiates ATP-driven DNA unwinding and endonuclease cleavage by the Mre11/Rad50 complex. *Genes Dev* 13: 1276–1288

Raymond WE, Kleckner N (1993) RAD50 protein of *Saccharomyces cerevisiae* exhibits ATP-dependent DNA binding. *Nucleic Acids Res* 21: 3851–3856

Reis CC, Batista S, Ferreira MG (2012) The fission yeast MRN complex tethers dysfunctional telomeres for NHEJ repair. *EMBO J* 31: 4576–4586

Rojowska A, Lammens K, Seifert FU, Direnberger C, Feldmann H, Hopfner KP (2014) Structure of the Rad50 DNA double-strand break repair protein in complex with DNA. *EMBO J* 33: 2847–2859

Schiller CB, Lammens K, Guerini I, Coordes B, Feldmann H, Schlauderer F, Möckel C, Schele A, Strässer K, Jackson SP, Hopfner KP (2012) Structure of Mre11-Nbs1 complex yields insights into ataxia-telangiectasia-like disease mutations and DNA damage signaling. *Nat Struct Mol Biol* 19: 693–700

Shibata A, Moiani D, Arvai AS, Perry J, Harding SM, Genois MM, Maity R, van Rossum-Fikkert S, Kertokalio A, Romoli F, Ismail A, Ismalaj E, Petricci E, Neale MJ, Bristow RG, Masson JY, Wyman C, Jeggo PA, Tainer JA (2014) DNA double-strand break repair pathway choice is directed by distinct MRE11 nuclease activities. *Mol Cell* 53: 7–18

Spell RM, Jinks-Robertson S (2004) Determination of mitotic recombination rates by fluctuation analysis in *Saccharomyces cerevisiae*. *Methods Mol Biol* 262: 3–12

Stewart GS, Maser RS, Stankovic T, Bressan DA, Kaplan MI, Jaspers NG, Raams A, Byrd PJ, Petrini JH, Taylor AM (1999) The DNA double-strand break repair gene hMre11 is mutated in individuals with an Ataxia-Telangiectasia-like disorder. *Cell* 99: 577–587

Stracker TH, Petrini JH (2011) The MRE11 complex, starting from the ends. *Nat Rev Mol Cell Biol* 12: 90–103

Sung S, Li F, Park YB, Kim JS, Kim AK, Song OK, Kim J, Che J, Lee SE, Cho Y (2014) DNA end recognition by the Mre11 nuclease dimer: insights into resection and repair of damaged DNA. *EMBO J* 33: 2422–2435

Symington LS, Gautier J (2011) Double-strand break end resection and repair pathway choice. *Annu Rev Genet* 45: 247–271

Trujillo KM, Sung P (2001) DNA structure-specific nuclease activities in the *Saccharomyces cerevisiae* Rad50/Mre11 complex. *J Biol Chem* 276: 35458–35464

Varon R, Vissinga C, Platzer M, Cerosaletti KM, Chrzanowska KH, Saar K, Beckmann G, Seemanová E, Cooper PR, Nowak NJ, Stumm M, Weemaes CM, Gatti RA, Wilson RK, Digweed M, Rosenthal A, Sperling K, Concannon P, Reis A (1998) Nibrin a novel DNA double-strand break repair protein is mutated in Nijmegen breakage syndrome. *Cell* 93: 467–476

Waltes R, Kalb R, Gatei M, Kijas AW, Stumm M, Sobeck A, Wieland B, Varon R, Lerenthal Y, Lavin MF, Schindler D, Dörk T (2009) Human RAD50 deficiency in a Nijmegen breakage syndrome-like disorder. *Am J Hum Genet* 84: 605–616

Williams RS, Moncalian G, Williams JS, Yamada Y, Limbo O, Shin DS, Groocock LM, Cahill D, Hitomi C, Guenther G, Moiani D, Carney JP, Russell P, Tainer JA (2008) Mre11 dimers coordinate DNA end bridging and nuclease processing in double-strand-break repair. *Cell* 135: 97–109

Williams GJ, Williams RS, Williams JS, Moncalian G, Arvai AS, Limbo O, Guenther G, SilDas S, Hammel M, Russell P (2011) ABC ATPase signature helices in Rad50 link nucleotide state to Mre11 interface for DNA repair. *Nat Struct Mol Biol* 18: 423–431

Yaffe MP, Schatz G (1984) Two nuclear mutations that block mitochondrial protein import in yeast. *Proc Natl Acad Sci USA* 81: 4819–4823

Zhu Z, Chung WH, Shim EY, Lee SE, Ira G (2008) Sgs1 helicase and two nucleases Dna2 and Exo1 resect DNA double-strand break ends. *Cell* 134: 981–994